Sensitive X-ray detectors made of methylammonium lead tribromide perovskite single crystals

Haotong Wei[1], Yanjun Fang[1], Padhraic Mulligan[2], William Chuirazzi[2], Hong-Hua Fang[3], Congcong Wang[4], Benjamin R. Ecker[4], Yongli Gao[4,5], Maria Antonietta Loi[3], Lei Cao[2]★ and Jinsong Huang[1]★

The large mobilities and carrier lifetimes of hybrid perovskite single crystals and the high atomic numbers of Pb, I and Br make them ideal for X-ray and gamma-ray detection. Here, we report a sensitive X-ray detector made of methylammonium lead bromide perovskite single crystals. A record-high mobility–lifetime product of 1.2×10^{-2} cm^2 V^{-1} and an extremely small surface charge recombination velocity of 64 cm s^{-1} are realized by reducing the bulk defects and passivating surface traps. Single-crystal devices with a thickness of 2–3 mm show 16.4% detection efficiency at near zero bias under irradiation with continuum X-ray energy up to 50 keV. The lowest detectable X-ray dose rate is 0.5 μGy$_{air}$ s^{-1} with a sensitivity of 80 μC Gy$_{air}^{-1}$ cm^{-2}, which is four times higher than the sensitivity achieved with α-Se X-ray detectors. This allows the radiation dose applied to a human body to be reduced for many medical and security check applications.

Sensitive and low-cost X-ray detectors have been actively sought for broad applications in the fields of security, defence, medical imaging, industrial material inspection, nuclear power stations and scientific research[1–3]. In all these applications high sensitivity is paramount, in that it allows the detection of a weaker X-ray dose rate and a smaller dose[4,5]. High-dose X-rays are known to be harmful to the human body, and an increased lifetime cancer risk is associated with X-ray inspections (for example, X-ray computed tomography), especially in children[6]. Enhancing the sensitivity of X-ray detectors can largely reduce such risks by minimizing the X-ray dose during routine medical inspections.

The operation of semiconductor-based X-ray detectors is similar to that of visible-light photodetectors in that a high signal-to-noise ratio is needed for high sensitivity. Their main differences are the photon energy absorbing process, charge generation process and the associated charge extraction process. Due to the much stronger penetration capability of X-ray photons, a much thicker active layer is needed to stop X-rays, and charges are generated across the entire thickness of the semiconductor crystal. To collect these charges it is necessary to have a large charge carrier mobility (μ)–charge carrier lifetime (τ) product (the mu–tau ($\mu\tau$) product), because the level of $\mu\tau$ determines the average carrier drift distance per unit electric field, and thus the charge collection efficiency at a given electric field. To this end, many photovoltaic semiconductors (such as Si, Cd (Zn)Te and Ge) have been studied for applications in radiation detection[4,7–11]. The X-ray stopping power (or attenuation coefficient α) of a material is very sensitive to atomic number Z, with the relation $\alpha \propto Z^4/E^3$ (ref. 12), where E is the X-ray photon energy. Although thick silicon single-crystalline detectors have been commercialized for X-ray detection because of their very

large $\mu\tau$ product, their sensitivity remains low due to the small Z of silicon.

Organolead trihalide perovskites (OTPs), which have emerged as a new generation of photovoltaic material and produced high power conversion efficiencies of around 20% within four years of their development[13–19], are also attractive for radiation detection because of their high-Z elements Pb, I and Br. Initial applications of methylammonium lead tri-iodide (MAPbI$_3$) perovskite films (thickness of 60 μm) in photoconductive devices have already been shown to be able to detect 8 keV soft X-rays[20], and a sensitivity of 1.1 μC Gy$_{air}^{-1}$ cm^{-2} for a perovskite photovoltaic device with a thickness of 600 nm was derived from the slope of the current output versus X-ray dose[20]. However, the polycrystalline films formed by spray coating in that work had a small $\mu\tau$ product of 2×10^{-7} cm^2 V^{-1}, which is five orders of magnitude smaller than that of state-of-the-art X-ray detector materials such as CdZnTe (refs 7,8). Another limitation of using thin-film perovskites for X-ray detection is the incomplete attenuation of the X-rays. Our simulation showed that thicknesses of 1.0 mm of MAPbI$_3$, 2.0 mm of MAPbBr$_3$ or 72.0 mm of silicon were needed to stop 98% of X-ray photons with an energy of 50 keV. Recent studies of OTP single crystals revealed dramatically enhanced carrier recombination lifetimes and carrier mobilities once the grain boundaries were removed[21–24], due to the 10^4 to 10^6 times smaller trap density. OTP single crystals combine the advantages of high stopping power, low trap density and high charge collection efficiency, which should enable high-sensitivity soft and hard X-ray detection.

In this Article, we report the first sensitive X-ray detector made of MAPbBr$_3$ single crystals. MAPbBr$_3$ was chosen for this study because its cubic crystal shape allows for easy electrode and device fabrication. We combine the crystal quality enhancement with
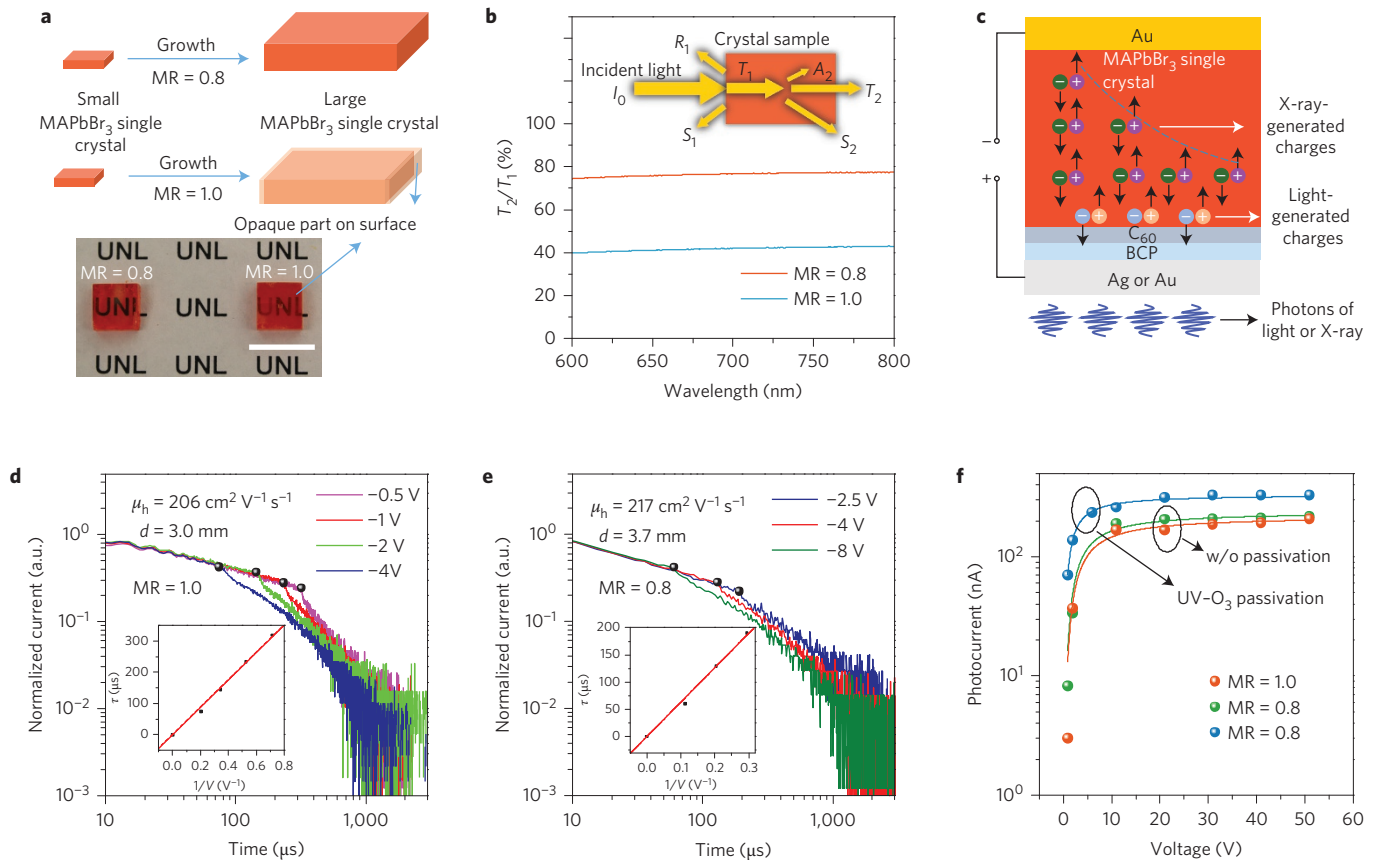
Figure 1 | Optoelectronic properties of MAPbBr₃ single crystals. a, Scheme and photograph of MAPbBr₃ single crystals with different molar ratios. Single crystal thickness (photograph), ~2 mm. Scale bar, 10 mm. **b**, Absolute transparency of 2-mm-thick single crystals synthesized with different precursor molar ratios. Inset: geometry of the light propagation process. R, S, T and A represent reflection, scattering, transmission and absorption, respectively. **c**, Single-crystal radiation detector structure. The charge generation regions are located close to the surface for visible light excitation and deeper inside the single crystal for X-ray excitation, respectively. **d,e**, Normalized transient current curves of MAPbBr₃ single-crystal devices with different molar ratios under various biases. Insets: charge transit time versus the reciprocal of bias (the solid line is a linear fit to the data). **f**, Photoconductivity of MAPbBr₃ single-crystal devices with different molar ratios and surface treatments. Fitting lines are also shown.

improved crystal growth, surface defect passivation by oxidization, and device interface engineering to fabricate a hard X-ray detector that can sense a very low X-ray dose rate with high sensitivity.

Non-stoichiometry precursor to improve the $\mu\tau$ product

A high-quality single crystal is needed to achieve a large $\mu\tau$ product. Here, the anti-solvent method developed by Bakr and colleagues was modified to grow high-quality MAPbBr₃ single crystals[24]. We found that single crystals grown with a lead bromide (PbBr₂)/methylamine bromine (MABr) molar ratio (MR) of 1.0 gradually changed from clear to opaque with this method. This is caused by the large difference in solubility between MABr and PbBr₂ in N,N-dimethylformamide (DMF), as shown in Supplementary Fig. 1a (PbBr₂ has a much lower solubility than MABr). After most of the DMF solvent is consumed by the anti-solvent, PbBr₂ precipitates faster than MABr, which might cause non-stoichiometric MAPbBr₃ or impurities on the surface (Supplementary Fig. 1b,c)[25]. To address this issue we used a molar ratio of 0.8 (so there was always more MABr in the solution); this resulted in the growth of clear single crystals with dimensions of 1–6 mm (Fig. 1a). In the following, we refer to crystals grown with PbBr₂/MABr molar ratios of 1.0 and 0.8 as MAPbBr₃–MR1.0 and MAPbBr₃–MR0.8, respectively. The absolute transparency (T_2/T_1) of these single crystals was quantitatively characterized by a spectrophotometer with an integration sphere, which accurately measures the transmittance, reflection and scattering of MAPbBr₃ single crystals (Supplementary Fig. 2). The set-up

for this measurement is shown in the inset of Fig. 1b. A high value of T_2/T_1 is expected for a clear crystal with less scattering and absorption from 600 to 800 nm. For the 2-mm-thick MAPbBr₃–MR0.8 and MAPbBr₃–MR1.0 single crystals, the values of T_2/T_1 were ~75% and ~40%, respectively (Fig. 1b), confirming visual observations. Powder X-ray diffraction (XRD) confirmed the cubic crystal structure of the MAPbBr₃–MR0.8 single crystals, and thermogravimetric analysis demonstrated an equimolar ratio composition of PbBr₂ and MABr in these single crystals (Supplementary Fig. 3a,b). A polarized optical microscopy image excluded the formation of polycrystals, and no holes or bubbles were observed inside the single crystals (Supplementary Fig. 3c,d). Larger single crystals have been synthesized with an area of 25 cm², paving the way for large-area array detector applications.

The electronic properties of the single crystals were characterized to determine the influence of the precursor molar ratios. The hole carrier mobilities of MAPbBr₃ single crystals were measured by a time-of-flight method. A MAPbBr₃ single-crystal device with the device structure Au/MAPbBr₃ single crystal/C₆₀/bathocuproine (BCP)/Ag or Au (Fig. 1c) was fabricated. The hole mobility of the MAPbBr₃–MR0.8 single crystal was found to be ~217 cm² V⁻¹ s⁻¹ (Fig. 1e), slightly higher than that of the MAPbBr₃–MR1.0 single crystal (206 cm² V⁻¹ s⁻¹) (Fig. 1d). A comparable electron mobility of 190 cm² V⁻¹ s⁻¹ was measured for the MAPbBr₃–MR0.8 single crystal (Supplementary Fig. 4). The $\mu\tau$ products of the single crystals were measured by the photoconductivity method, which is generally
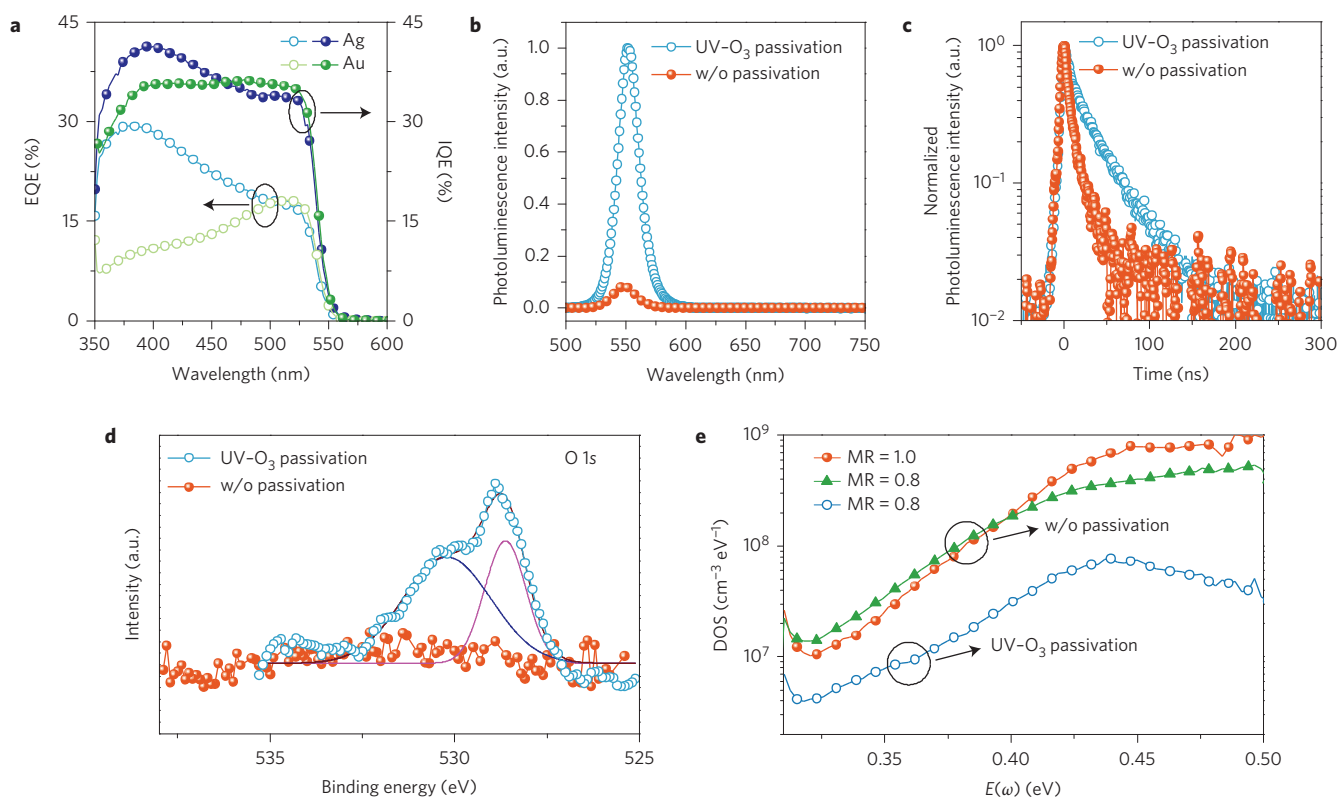
Figure 2 | UV–O$_3$ passivation of the surface traps of MAPbBr$_3$ single crystals. a, EQE and IQE of the MAPbBr$_3$ single-crystal devices with different cathode electrodes after UV–O$_3$ passivation. **b**, Photoluminescence spectra of a MAPbBr$_3$ single crystal in vacuum before and after UV–O$_3$ treatment. **c**, Photoluminescence lifetime of the MAPbBr$_3$ single crystal in vacuum before and after UV–O$_3$ treatment. **d**, XPS spectra of the MAPbBr$_3$ thin film for O 1s before and after UV–O$_3$ passivation. **e**, Trap density of states of the MAPbBr$_3$ single-crystal devices with different molar ratios, before and after UV–O$_3$ treatment.

applied to single-crystal radiation detection and also gives the surface recombination velocity s (refs 26,27). The measured photocurrent was fit to the modified Hecht equation[26,27]:

$$I = \frac{I_0 \mu \tau V}{L^2} \frac{1 - \exp\left(-\frac{L^2}{\mu \tau V}\right)}{1 + \frac{L}{V}\frac{s}{\mu}} \qquad (1)$$

where I_0 is the saturated photocurrent, L is the thickness, and V is the applied bias. The measured photocurrent curves (and fitting curves) are shown in Fig. 1f. The MAPbBr$_3$–MR1.0 single crystal has a $\mu\tau$ product of 1.0×10^{-2} cm^2 V^{-1} and s of 1,680 cm s^{-1}, and the MAPbBr$_3$–MR0.8 single crystal has a record $\mu\tau$ product of 1.4×10^{-2} cm^2 V^{-1} and a lower s of 1,120 cm s^{-1}. According to a carrier recombination lifetime study using microwave photoconductivity measurements[28], the $\mu\tau$ product measured here should be dominated by the contribution from holes because of the shorter recombination lifetime of electrons than holes. This surface recombination velocity agrees surprisingly well with what was measured by the broadband transient reflectance spectroscopy method[23]. All these results indicate that growing MAPbBr$_3$ single crystals with more MABr yields better crystals with improved optical and electronic properties. The hole diffusion length L_D was derived to be 190 μm for the MAPbBr$_3$–MR0.8 single crystal, which is of the same order as that reported previously for MAPbI$_3$ single crystals[21].

Surface passivation to enhance charge extraction efficiency

We found there was a large density of surface defects in as-grown OTP single crystals, which led to the narrowband light-detection

characteristics in our previous study[29]. Although the single crystal growth method applied here yielded a reduced surface defect density, there were still a significant number of surface defects in these as-grown MAPbBr$_3$ single crystals, as evidenced by the large surface recombination velocity measured and the relative small internal quantum efficiency (IQE) at short wavelength range (Supplementary Fig. 5). Interestingly, we found that UV–O$_3$ treatment of the top surface of an as-grown MAPbBr$_3$ single crystal for 20 min increased the external quantum efficiency (EQE) and IQE of MAPbBr$_3$ single-crystal devices at short wavelengths (Fig. 2a), which indicates that oxidization can effectively passivate these surface defects. This passivation effect was directly confirmed by measuring the photoluminescence, which is sensitive to surface defects due to the short penetration length of the short-wavelength excitation light (405 nm). As shown in Fig. 2b,c, the oxidized MAPbBr$_3$–MR0.8 single crystals have 12 times stronger photoluminescence intensity and three times longer radiative recombination lifetime than pristine MAPbBr$_3$ single crystals under vacuum condition. Additional evidence of the oxidative passivation of the trap states is that the photoluminescence of pristine MAPbBr$_3$ is also intense in air (unpublished result). X-ray photoelectron spectrometer (XPS) measurements were carried out to verify the retention of the oxidization effect by UV–O$_3$ treatment. A MAPbBr$_3$ thin film was used instead of a single crystal to avoid the charging effect caused by the large thickness of the single crystal. As shown in Fig. 2d, oxygen 1s peaks show up after UV–O$_3$ passivation, indicating that the high-vacuum environment in XPS measurements could not remove the chemically attached oxygen species. This verifies the permanent passivation effect of UV–O$_3$ passivation, which is in accordance with the photoluminescence variation. The peak at 528.7 eV is attributed to oxygen atoms bonded to lead, while the
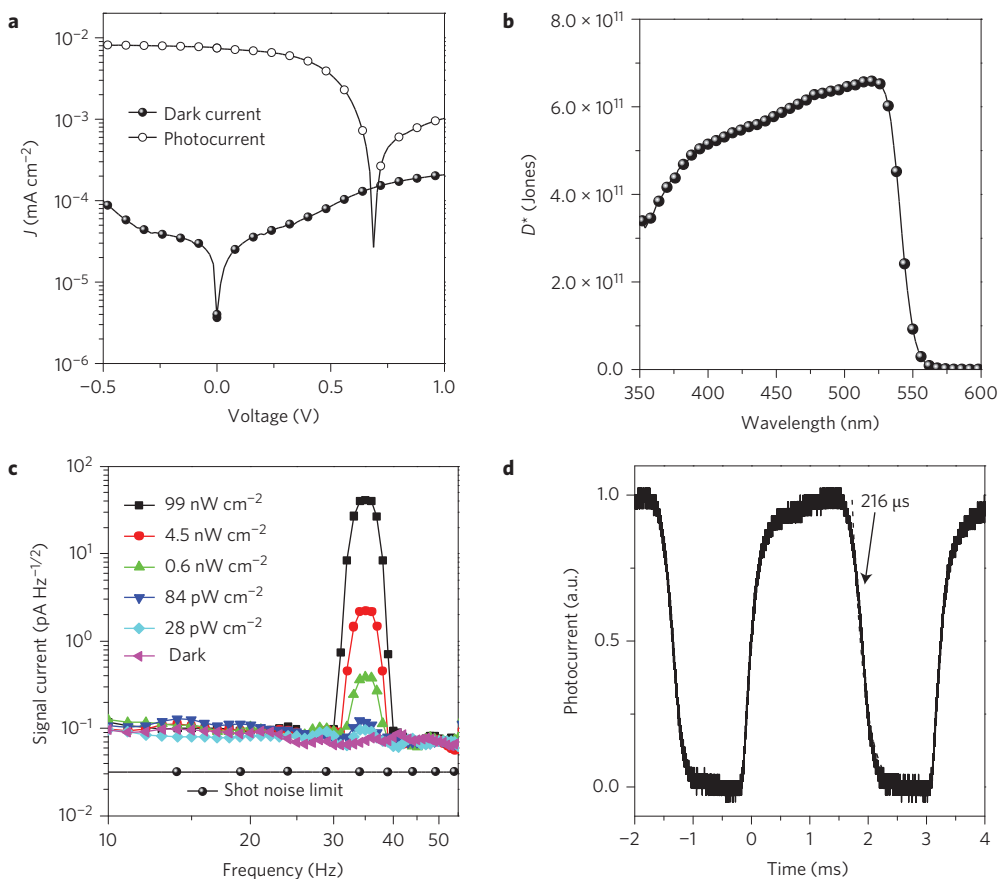
Figure 3 | Photodetection performance of the MAPbBr$_3$ single-crystal devices. a, Dark current and photocurrent of the MAPbBr$_3$ single-crystal device. **b**, Specific detectivity of the MAPbBr$_3$ single-crystal device calculated from the directly measured IQE and NEP. **c**, Noise current and photocurrent for the MAPbBr$_3$ single-crystal device under −0.1 V bias at different frequencies. The light source is a 470 nm light-emitting diode, modulated at 35 Hz by a functional generator, with light intensity attenuated by neutral density filters. **d**, Temporal response of the MAPbBr$_3$ single-crystal device with a thickness of 1 mm under −0.1 V bias.

peak centred at 530.3 eV arises from those forming hydroxyl bonds[30,31]. The passivation of perovskite by oxygen was predicted previously from Yan's calculation[32], and is observed for the first time here. After UV–O$_3$ passivation, the MAPbBr$_3$–MR0.8 single crystals had an 18 times slower surface recombination velocity of 64 cm s^{-1} (Fig. 1f), which is even better than that of state-of-the-art passivated silicon[33]. The $\mu\tau$ product remained unchanged after passivation, which is reasonable because it is a bulk property. The trap density of states (tDOS) of MAPbBr$_3$ single crystals was characterized by thermal admittance spectroscopy. As shown in Fig. 2e, the trap density of the MAPbBr$_3$–MR0.8 single-crystal device is similar to that of the MAPbBr$_3$–MR1.0 device in most trap-depth ranges, but is about twice as low for deep traps, which again indicates the origin of deep traps as being the crystal surfaces. The trap density of the MAPbBr$_3$ single crystal was reduced by approximately tenfold after passivation by UV–O$_3$, yielding a trap density of between 3×10^6 and 7×10^7 cm^{-3} eV^{-1}, which is the lowest measured trap density of all known single crystals. It should be noted this is an average trap density and the surface trap density should be much higher than that in the bulk.

Surface passivation by oxidization successfully increased the device charge extraction efficiency. Because the EQE spectra of the devices are sensitive to the transparency of the semitransparent electrodes, we compared the performance of the devices using 14 nm silver or 25 nm gold as the cathode. Thinner silver could be used because of its better film formation capability on single crystals, and the high work function of gold worked for the cathode due

to the C$_{60}$/BCP electron-accepting layer inserted between the perovskite and gold. Because the 14 nm silver electrode has a transparency of ~80–50% from 350 to 600 nm, the IQE is 33–42% on average from 350 to 520 nm, which is close to the IQE of the device with gold as the cathode. This means that, of all the holes generated by the energy of the absorbed photons, more than one-third of these charge carriers can diffuse and/or drift across the entire 2 mm crystal under −0.1 V bias. The device charge extraction efficiency doubled with UV–O$_3$ passivation (Fig. 2a and Supplementary Fig. 5), and the presence of large IQE and EQE for the short wavelength region indicates reduced charge recombination closing to the semitransparent cathode. It should be noted that the electric field intensity applied here is several orders of magnitude lower than that used for polycrystalline perovskite films to minimize the possible influence of ion migration or an electrochemical reaction[34], despite the fact that a larger IQE (close to 100%) could be realized at a larger bias of −8 V (Supplementary Fig. 5).

Photodetectors and X-ray detectors
The sensitivity of the 2-mm-thick MAPbBr$_3$–MR0.8 single-crystal device under weak light was characterized. The device showed a small dark-current density of 29 nA cm^{-2} at −0.1 V bias, which gives a bulk resistivity of 1.7×10^7 Ω cm for the MAPbBr$_3$–MR0.8 single crystal. The device also showed a photovoltaic behaviour with a short-circuit current density of ~7.8×10^{-3} mA cm^{-2} under ambient light (~2.2×10^{-4} W cm^{-2}) (Fig. 3a) and an open-circuit-voltage of 686 mV. A maximum specific detectivity D^* of
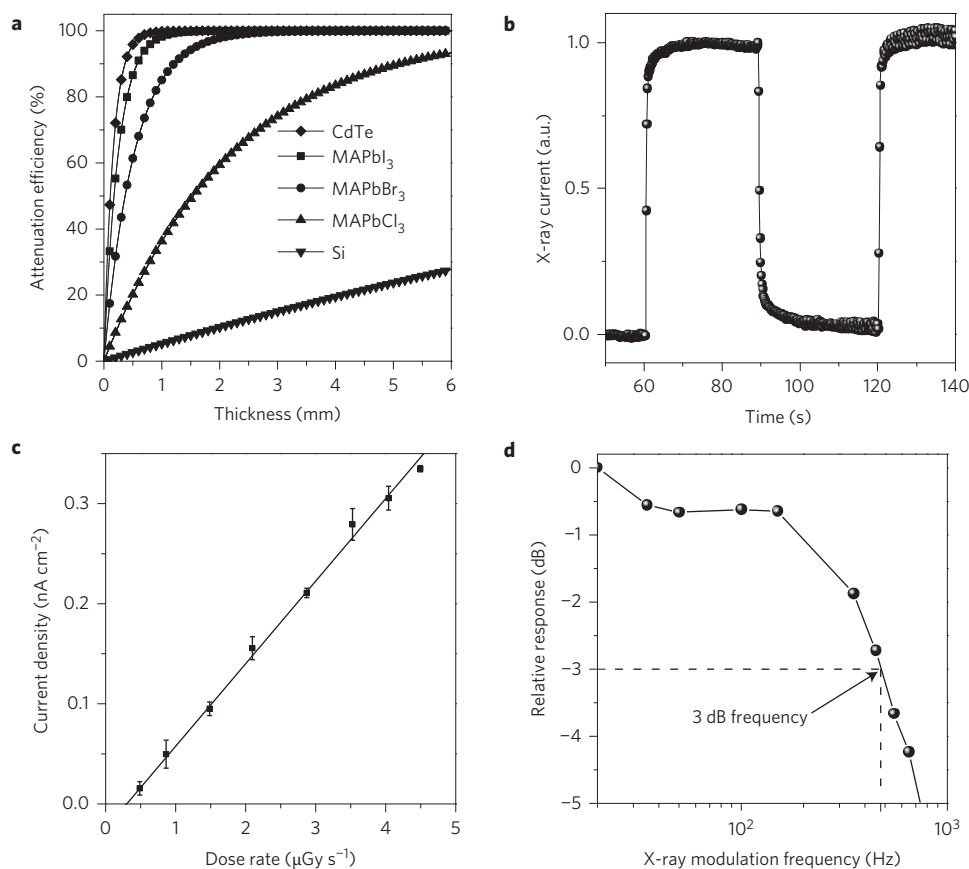
Figure 4 | X-ray detection performance of the MAPbBr$_3$ single-crystal devices. a, Attenuation efficiency of CdTe, MAPbI$_3$, MAPbBr$_3$, MAPbCl$_3$ and silicon to 50 keV X-ray photons (in terms of the photoelectric effect) versus thickness. **b**, MAPbBr$_3$ single-crystal device response to X-rays by turning the X-ray source on and off. **c**, X-ray-generated photocurrent at various dose rates, down to the lowest detectable dose rate. A sensitivity of 80 μC Gy$_{air}^{-1}$ cm^{-2} is derived from the slope of the fitting line. **d**, Normalized response as a function of input X-ray frequency showing that the 3 dB cutoff frequency is 480 Hz.

6.6×10^{11} cm Hz$^{1/2}$ W^{-1} (Fig. 3b) is derived from the noise current (Fig. 3c) and IQE (Fig. 2a)[35], which gives a noise-equivalent power (NEP) of ~10 pW cm^{-2}. The noise current is independent of the frequency and close to the calculated shot noise limit from the dark current[35]. White noise, instead of $1/f$ noise, dominates the total noise due to the low bulk trap density of the perovskite single crystals. We verified the NEP by directly measuring the device response to light intensity varying from 100 nW cm^{-2} to 28 pW cm^{-2}, using a combination of a fast Fourier transform (FFT) signal analyser and a low-noise current preamplifier[36]. As shown in Fig. 3c, the device signal is distinguished from noise when the light intensity reduces to 28 pW cm^{-2}, which is close to the calculated NEP. Due to the large charge carrier mobility of MAPbBr$_3$ single crystals, the detector shows a relatively short response time of 216 μs for the device with a 1-mm-thick single-crystal device under −0.1 V (Fig. 3d) and 1.1 ms for the 2.6-mm-thick single-crystal device (Supplementary Fig. 6). The transit times of the charge carriers calculated with the measured mobilities for 1 mm and 2.6 mm devices are 200 μs and 1.3 ms, respectively, which agree well with the measured response times.

We exposed our 2-mm-thick MAPbBr$_3$ single-crystal device to an X-ray source with a continuum X-ray energy up to 50 keV and peak intensity at 22 keV, for which the radiation dose rate was calibrated by a silicon detector. The X-ray source was a commercially available Amptek Mini-X tube, with a silver target and 4 W maximum power output. X-rays from the source were collimated using a brass cylinder with a 2-mm-diameter circular central bore. Spectra at the sample location were characterized using a cooled high-resolution Si-PIN detector with an additional tungsten

aperture with a 0.4-mm-diameter hole and a function was determined to correlate the X-ray generator voltage and current to the kinetic energy released per unit mass (KERMA) in a sample. Mass energy attenuation coefficients from a photon cross-section database[37] were used to determine the KERMA in the OTP samples. The stopping power of OTPs is similar to that of CdTe, but much stronger than that of silicon due to the enhanced photoelectric absorption, as shown by the simulation results in Fig. 4a. The 2-mm-thick MAPbBr$_3$ used in this work attenuated almost all of the X-rays within the energy range of the X-ray source used. The very thin gold or silver electrode contributes negligible X-ray attenuation. The response of the single-crystal devices to X-rays was demonstrated by turning the incident X-rays on and off, as shown in Fig. 4b.

The sensitivity and lowest detectable dose rate are the most important figures of merit to evaluate the performance of an X-ray detector for medical imaging applications. To evaluate these, the total X-ray dose was reduced by a tungsten aperture with a diameter of 0.4 mm to control the X-ray beam size, as well as by changing the current of the X-ray tube. We applied the same method as used in light detection for X-ray detection; that is, the X-ray intensity was modulated by a thick steel chopper and the current signal of the single-crystal device was measured by a lock-in amplifier at the same frequency of the chopped X-ray. As shown in Fig. 4c, the generated current density signal has a linear relationship with the X-ray dose rate. The dose used here is the entrance dose in air, and a sensitivity of 80 μC Gy$_{air}^{-1}$ cm^{-2} was derived, which is more than ten times higher than that of the Cd(Zn)Te single-crystal detector under the same applied electrical

field[38]. Note that, although a larger applied field was reported to enhance the current output of the Cd(Zn)Te single-crystal detectors[38,39], the sensitivities, which are determined by the signal-to-noise ratio, are not enhanced due to the increased dark current at higher bias. We also compared the sensitivity of the perovskite devices with the sensitivity of α-Se X-ray detectors, which are the dominating products for X-ray imaging. The MAPbBr$_3$ single-crystal detectors are four times more sensitive than the α-Se X-ray detectors operating at a much higher field of 10 V μm^{-1} (20 μC Gy$_{air}^{-1}$ cm^{-2})[5]. In addition, compared with the polycrystalline perovskite X-ray detectors[20], the sensitivity improved by more than 70 times, despite the much smaller bias applied, which clearly reveals the advantage of the application of high-$\mu\tau$-product MAPbBr$_3$ single crystals for X-ray detectors. The lowest detectable X-ray dose rate is 0.5 μGy$_{air}$ s^{-1} at near zero bias, which is much lower than that required for regular medical diagnostics (5.5 μGy$_{air}$ s^{-1}; refs 40,41).

An estimation of the charge collection efficiency was determined for the device under an X-ray dose rate of 0.86 μGy$_{air}$ s^{-1} by considering the average energy of the X-ray beam to be 22 keV. The electron–hole pair creation energy W is predicted to be 6.03 eV according to the empirical model of Devanathan and co-authors[42]:

$$W = 2E_g + 1.43 \qquad (2)$$

where E_g is the bandgap of MAPbBr$_3$. We derived a charge collection efficiency of 16.4%, which is a little lower than the IQE of ~33–42% measured under UV–vis photons. In principle, both electrons and holes may contribute to the signal under X-rays if the lifetime of the electrons is as large as that of the holes. However, our carrier lifetime study using microwave photoconductivity measurements showed that electrons have a much shorter lifetime, especially at very weak light intensities[28]. Because the X-ray intensity used in this study is also weak compared with sunlight, we speculated that the major contribution to the signal comes from holes for devices measured under X-rays. The derived charge collection efficiency of the nearly zero-biased device under very weak X-ray illumination is a result of the very low trap density of the single crystals. For the 2-mm-thick device, the measured 3 dB cutoff frequency (f_{3dB}) response to X-rays is 480 Hz (Fig. 4d)—that is, a response time of 730 μs—which is faster than that estimated from the calculated charge transit time of 800 μs. This can be explained by the fact that charges are generated inside the crystals by X-ray radiation and thus the actual charge transit length is smaller than the crystal thickness. Device stability is another important figure-of-merit. The MAPbBr$_3$ single-crystal device is very stable without obvious EQE loss after being stored in air for two months (Supplementary Fig. 7). The EQE measurement for the devices was carried out under ambient air conditions, without any protection.

In conclusion, we have fabricated sensitive MAPbBr$_3$ single-crystal X-ray detectors with a record $\mu\tau$ product of 1.2×10^{-2} cm^2 V^{-1} and the lowest surface recombination velocity of 64 cm s^{-1}. It is impressive to achieve such extraordinary optoelectronic properties from solution-grown perovskite single crystals and with such a simple surface passivation treatment compared with those for CdZnTe. The solution growth method has the unprecedented advantages of low cost, large scale and faster growth rates than the vapour deposition, travelling heater or Bridgman method adopted for CdZnTe crystal growth. This could potentially result in low-cost and sensitive radiation detectors to be deployed in the field for a wide range of applications. Using these MAPbBr$_3$ single-crystal X-ray detectors, we have demonstrated a charge collection efficiency of up to ~33–42% for UV–vis light, and ~16.4% for hard X-ray photons at a near zero bias condition. This facilitates the capability

to directly convert high-energy X-ray flux into collectable charges with a high sensitivity of 80 μC Gy$_{air}^{-1}$ cm^{-2} and a lowest detectable dose rate of 0.5 μGy$_{air}$ s^{-1}, which meets the practical needs of medical diagnostics where the dose rate is typically much larger than this[40,41]. Better device performance can be expected if the surface traps are further passivated and the possible ion-migration problem is avoided so that a larger bias can be applied to extract more charges at a quicker rate. The findings also offer an effective way to engineer the trap density of the hybrid perovskite material to increase the device charge collection efficiency for other applications, including solar cells and photodetectors.

Methods

Methods and any associated references are available in the online version of the paper.

References

1. Kasap, S. et al. Amorphous and polycrystalline photoconductors for direct conversion flat panel X-ray image sensors. *Sensors* **11,** 5112–5157 (2011).
2. Yaffe, M. J. & Rowlands, J. A. X-ray detectors for digital radiography. *Phys. Med. Biol.* **42,** 1–39 (1997).
3. Tegze, M. & Faigel, G. X-ray holography with atomic resolution. *Nature* **380,** 49–51 (1996).
4. Shah, K. S. et al. X-ray imaging with PbI$_2$-based a-Si:H flat panel detectors. *Nucl. Instrum. Methods Phys. Res. A* **458,** 140–147 (2001).
5. Kasap, S. O. X-ray sensitivity of photoconductors: application to stabilized a-Se. *J. Phys. D* **33,** 2853 (2000).
6. Brenner, D. J., Elliston, C. D., Hall, E. J. & Berdon, W. E. Estimated risks of radiation-induced fatal cancer from pediatric CT. *Am. J. Roentgenol.* **176,** 289–296 (2001).
7. Eisen, Y. & Shor, A. CdTe and CdZnTe room-temperature X-ray and gamma ray detectors and imaging systems. *IEEE Trans. Nucl. Sci.* **487,** 1191–1198 (2004).
8. Szeles, C. CdZnTe and CdTe materials for X-ray and gamma ray radiation detector applications. *Phys. Status Solidi* **241,** 783–790 (2004).
9. Kabir, M. Z. & Kasap, S. O. Charge collection and absorption-limited sensitivity of X-ray photoconductors: applications to a-Se and HgI$_2$. *Appl. Phys. Lett.* **80,** 1664–1666 (2002).
10. Luke, P. N., Rossington, C. S. & Wesela, M. F. Low energy X-ray response of Ge detectors with amorphous Ge entrance contacts. *IEEE Trans. Nucl. Sci.* **41,** 1074–1079 (1994).
11. Jeong, M., Jo, W. J., Kim, H. S. & Ha, J. H. Radiation hardness characteristics of Si-PIN radiation detectors. *Nucl. Instrum. Methods Phys. Res. A* **784,** 119–123 (2015).
12. Evans, R. D. & Noyau, A. *The Atomic Nucleus* Vol. 582 (McGraw-Hill, 1955).
13. Bi, C. et al. Non-wetting surface-driven high-aspect-ratio crystalline grain growth for efficient hybrid perovskite solar cells. *Nature Commun.* **6,** 7747 (2015).
14. Jeon, N. J. et al. Compositional engineering of perovskite materials for high-performance solar cells. *Nature* **517,** 476–480 (2015).
15. Liu, M., Johnston, M. B. & Snaith, H. J. Efficient planar heterojunction perovskite solar cells by vapour deposition. *Nature* **501,** 395–398 (2013).
16. Yang, W. S. et al. High-performance photovoltaic perovskite layers fabricated through intramolecular exchange. *Science* **348,** 1234–1237 (2015).
17. Zhou, H. et al. Interface engineering of highly efficient perovskite solar cells. *Science* **345,** 542–546 (2014).
18. Burschka, J. et al. Sequential deposition as a route to high-performance perovskite-sensitized solar cells. *Nature* **499,** 316–319 (2013).
19. Xing, G. et al. Long-range balanced electron- and hole-transport lengths in organic–inorganic CH$_3$NH$_3$PbI$_3$. *Science* **342,** 344–347 (2013).
20. Yakunin, S. et al. Detection of X-ray photons by solution-processed lead halide perovskites. *Nature Photon.* **9,** 444–449 (2015).
21. Dong, Q. et al. Electron–hole diffusion lengths >175 μm in solution-grown CH$_3$NH$_3$PbI$_3$ single crystals. *Science* **347,** 967–970 (2015).
22. Saidaminov, M. I. et al. High-quality bulk hybrid perovskite single crystals within minutes by inverse temperature crystallization. *Nature Commun.* **6,** 7586 (2015).
23. Yang, Y. et al. Low surface recombination velocity in solution-grown CH$_3$NH$_3$PbBr$_3$ perovskite single crystal. *Nature Commun.* **6,** 7961 (2015).
24. Shi, D. et al. Low trap-state density and long carrier diffusion in organolead trihalide perovskite single crystals. *Science* **347,** 519–522 (2015).
25. Castelli, I. E., Thygesen, K. S. & Jacobsen, K. W. Calculated optical absorption of different perovskite phases. *J. Mater. Chem. A* **3,** 12343–12349 (2015).
26. Androulakis, J. et al. Dimensional reduction: a design tool for new radiation detection materials. *Adv. Mater.* **23,** 4163–4167 (2011).

27. Stoumpos, C. C. *et al.* Crystal growth of the perovskite semiconductor CsPbBr₃: a new material for high-energy radiation detection. *Cryst. Growth Des.* **13**, 2722–2727 (2013).

28. Bi, Y. *et al.* Charge carrier lifetimes exceeding 15 μs in methylammonium lead iodide single crystals. *J. Phys. Chem. Lett.* **7**, 923–928 (2016).

29. Fang, Y. *et al.* Highly narrowband perovskite single-crystal photodetectors enabled by surface-charge recombination. *Nature Photon.* **9**, 679–686 (2015).

30. Hsieh, P. T., Chen, Y. C., Kao, K. S. & Wang, C. M. Luminescence mechanism of ZnO thin film investigated by XPS measurement. *Appl. Phys. A* **90**, 317–321 (2008).

31. Casalongue, H. S. *et al.* Direct observation of the oxygenated species during oxygen reduction on a platinum fuel cell cathode. *Nature Commun.* **4**, 2817 (2013).

32. Yin, W.-J. *et al.* Origin of high electronic quality in structurally disordered CH₃NH₃PbI₃ and the passivation effect of Cl and O at grain boundaries. *Adv. Electron. Mater.* **1**, 1500044 (2015).

33. Schmidt, J. *et al.* Surface passivation of high-efficiency silicon solar cells by atomic-layer-deposited Al₂O₃. *Prog. Photovoltaics* **16**, 461–466 (2008).

34. Xiao, Z. *et al.* Giant switchable photovoltaic effect in organometal trihalide perovskite devices. *Nature Mater.* **14**, 193–198 (2015).

35. Guo, F. *et al.* A nanocomposite ultraviolet photodetector based on interfacial trap-controlled charge injection. *Nature Nanotech.* **7**, 798–802 (2012).

36. Wei, H. *et al.* Trap engineering of CdTe nanoparticle for high gain, fast response, and low noise P3HT:CdTe nanocomposite photodetectors. *Adv. Mater.* **27**, 4975–4981 (2015).

37. Berger, M. J. *et al. XCOM: Photon Cross Sections Database: NIST Standard Reference Database 8* (NIST, 2013).

38. Dvoryankin, V. F. *et al.* X-ray sensitivity of Cd₀.₉Zn₀.₁Te detectors. *Tech. Phys.* **55**, 306–308 (2010).

39. Schieber, M. *et al.* Theoretical and experimental sensitivity to X-rays of single and polycrystalline HgI₂ compared with different single-crystal detectors. *Nucl. Instrum. Methods Phys. Res. A* **458**, 41–46 (2001).

40. Shearer, D. R. & Bopaiah, M. Dose rate limitations of integrating survey meters for diagnostic X-ray surveys. *Health Phys.* **79**, S20–S21 (2000).

41. Clairand, I. *et al.* Use of active personal dosemeters in interventional radiology and cardiology: tests in laboratory conditions and recommendations—ORAMED project. *Radiat. Meas.* **46**, 1252–1257 (2011).

42. Devanathan, R., Corrales, L. R., Gao, F. & Weber, W. J. Signal variance in gamma-ray detectors—a review. *Nucl. Instrum. Methods Phys. Res. A* **565**, 637–649 (2006).

Acknowledgements

Author contributions

J.H. conceived and supervised the project. H.W. synthesized materials, fabricated the device and measured the optoelectronic properties and photodetector performance. P.M., W.C. and L.C. measured the device properties under X-ray radiation. H.W., Y.F. and P.M. calculated the charge collection efficiency under X-ray radiation. H.H.F. and M.A.L. performed photoluminescence and photoluminescence lifetime measurements. C.W., B.E. and Y.G. carried out XPS measurement. All authors analysed the data. J.H. and H.W. wrote the manuscript, and all authors reviewed it.

Additional information

Supplementary information is available in the online version of the paper. Reprints and permissions information is available online at www.nature.com/reprints. Correspondence and requests for materials should be addressed to J.H. and L.C.

Competing financial interests

The authors declare no competing financial interests.

Methods

Materials. Lead bromide ($PbBr_2$, >98%) and BCP (>96%) were purchased from Sigma-Aldrich, methylamine (CH_3NH_2, 40% wt/wt aq. sol.), hydrobromic acid (HBr, 48% wt/wt aq. sol.), N,N-dimethylformamide (DMF, >99.8%) and dichloromethane (DCM, 99.7%) from Alfa Aesar, and C_{60} (>99.5%) from Nano-C.

Synthesis of methylamine bromine (MABr). MABr was prepared by slowly mixing methylamine with HBr in a 1:1 molar ratio under continuous stirring at 0 °C for 2 h. MABr was then crystallized by removing the solvent from an evaporator, washing three times in diethyl ether and filtering the precipitate. The white crystal was obtained by recrystallization with ethanol, then dried in vacuum for 24 h and kept in a dark and dry environment for further use.

Growth of MAPbBr₃ single crystal. $PbBr_2$ (0.64 M) and MABr (0.8 M) were dissolved in 5 ml DMF solution in a 20 ml vial to obtain a 0.8 molar ratio of $PbBr_2$ to MABr. The vial was then sealed with foil, except for a small hole to allow the DCM to slowly enter. DCM was used as an anti-solvent to precipitate the single crystals. The vial was then stored in an atmosphere of DCM, and the MAPbBr₃–MR0.8 single crystals slowly grew over two days. A 1.0 molar ratio of $PbBr_2$ to MABr was also used to grow MAPbBr₃–MR1.0 single crystals, for comparison.

Optical measurements. The absolute transparency was characterized using T_2/T_1, where T_1 and T_2 are the injected and transmitted light, into and out of the single crystals, respectively. We demonstrated absolute transparency in the wavelength range from 600 to 800 nm, where the crystal has no band transition.

Device fabrication. A gold (25 nm) anode was deposited on the top surface of the MAPbBr₃ single crystal by thermal evaporation, using a mask to define the area. Electron-transporting layers were then constructed on the bottom surface by depositing 20 nm C_{60} and 8 nm BCP. Finally, a 14 nm silver or 25 nm gold semi-transparent cathode was deposited using a thermal evaporation system through a shadow mask under high vacuum. For the UV–O_3 passivation device, the top surface of the MAPbBr₃ single crystal was treated by UV–O_3 for 20 min before depositing the anode electrode. The device area varied from 4 to 16 mm^2 depending on the size of the MAPbBr₃ single crystals.